PROCEEDINGS OF SPIE

SPIEDigitalLibrary.org/conference-proceedings-of-spie

Modally selective nonlinear ultrasonic waves for characterization of pitting damage in whipple shields of spacecraft

Cao, Wuxiong, Wang, Kai, Xu, Lei, Zhou, Pengyu, Yang, Xiongbin, et al.

Wuxiong Cao, Kai Wang, Lei Xu, Pengyu Zhou, Xiongbin Yang, Baojun Pang, Paul Fromme, Zhongqing Su, "Modally selective nonlinear ultrasonic waves for characterization of pitting damage in whipple shields of spacecraft," Proc. SPIE 11381, Health Monitoring of Structural and Biological Systems XIV, 113811M (22 April 2020); doi: 10.1117/12.2557716

SPIE.

Event: SPIE Smart Structures + Nondestructive Evaluation, 2020, Online Only

Downloaded From: https://www.spiedigitallibrary.org/conference-proceedings-of-spie on 07 Jul 2020 Terms of Use: https://www.spiedigitallibrary.org/terms-of-use

Modally Selective Nonlinear Ultrasonic Waves for Characterization of Pitting Damage in Whipple Shields of Spacecraft

Wuxiong Cao[a,b], Kai Wang[b], Lei Xu[b], Pengyu Zhou[b], Xiongbin Yang[b], Baojun Pang[a], Paul Fromme[c], and Zhongqing Su*[b,d]
[a]School of Astronautics, Harbin Institute of Technology, Harbin 150080, P.R. China
[b]Department of Mechanical Engineering, The Hong Kong Polytechnic University, Hung Hom Kowloon, Hong Kong SAR
[c]Department of Mechanical Engineering, University College London, London, United Kingdom
[d]The Hong Kong Polytechnic University Shenzhen Research Institute, Shenzhen 518057, P.R. China

ABSTRACT

Featuring hundreds of craters, cracks and diverse microscopic defects disorderedly scattered over a wide region, the pitting damage in a typical Whipple shield of spacecraft induces highly complex wave scattering. Due to the dispersive and multimode natures, only nonlinear ultrasonic waves (NUWs) with exact phase-velocity matching condition are generally used to evaluate the microstructural material deterioration. Targeting accurate, holistic evaluation of pitting damage, semi-analytical finite element (SAFE) approach is adopted to identify the internal resonant conditions and to select an efficient mode pair for characterizing pitting damage. To explore the feasibility of pitting damage evaluation by using the selected mode pair and fully utilize its unique merits, the cumulative effect of second harmonics is analyzed using numerical simulations and corroborated by experiment. Regardless of the selection of mode pair (*i.e.*, S1-s2 and S0-s0), the amplitude of second harmonics obtained in the pitted plate is observed to increase significantly after the probing GUWs traverse the pitted region, upon interacting with the pitting damage. This phenomenon is remarkable particularly when the probing GUW does not satisfy the requirement of internal resonance. The mode pairs S0-s0 with different degrees of phase-velocity mismatching are further analyzed. Results show that the hypervelocity impact-induced pitting damage in the rear wall of Whipple shields can be detected accurately using the mode pair S0-s0, and a relatively higher excitation frequency is preferred due to its higher degree of phase-velocity mismatching, leading to standing out of the pitting damage-induced CAN.

Keywords: Pitting damage, semi-analytical finite element, nonlinear ultrasonic waves, mode selection, spacecraft

1. INTRODUCTION

Amongst countless micrometeoroids/orbital debris (MMOD) that are cluttering in low Earth orbit (LEO), over 23,000 of them are larger than 5 cm and traceable, which are mingled with another ~750,000 colloquially called "flying bullets" sized between 1 and 5 cm. MMOD smaller than 1 cm are estimated to be ~170 million. MMOD are flying around Earth at speeds over 7.9 km/s (*i.e.*, the first cosmic velocity)[1,2]. An MMOD particle beyond 10 mm diameter can penetrate the bumper layer of a Whipple shield, owing to its kinetic energy. As a result, debris cloud is produced which subsequently impinges on the rear wall of spacecraft to cause pitting damage. Material degradation and deterioration caused by pitting damage, usually initiated at an unperceivable scale but progressing at an alarming speed, can fairly compromise structural reliability, integrity and performance, and without timely awareness lead to fragmentation and even failure of the entire system. This has entailed early detection of pitting damage and accurate assessment of its severity, on which basis follow-up remedial measures can be implemented. However, evaluation of pitting damage is far beyond the detectability of conventional approaches using guided ultrasonic waves (GUWs), because the large number of craters and cracks within the pitting area (Figure 1) cause highly complex, mutually-interfering wave scattering, making signal interpretation a daunting task. This has created a clear impasse to GUW-based inspection when used to detect pitting damage, let alone extending off-line detection of pitting damage to on-line, continuous monitoring of its deterioration[3].

* Zhongqing.Su@polyu.edu.hk; phone: +852-2766-7818; fax: +852-2365-4703

Health Monitoring of Structural and Biological Systems XIV, edited by Paul Fromme, Zhongqing Su, Proc. of SPIE Vol. 11381, 113811M · © 2020 SPIE
CCC code: 0277-786X/20/$21 · doi: 10.1117/12.2557716

Downloaded From: https://www.spiedigitallibrary.org/conference-proceedings-of-spie on 07 Jul 2020
Terms of Use: https://www.spiedigitallibrary.org/terms-of-use

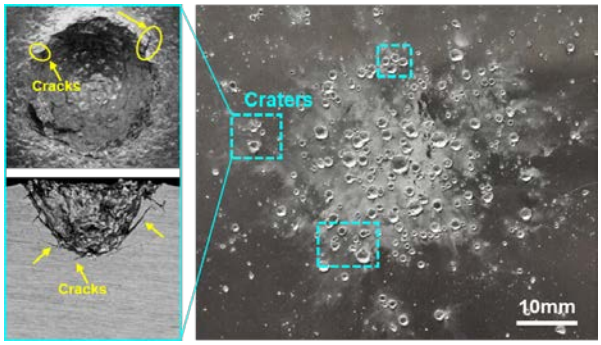

Figure 1. Hypervelocity impact (HVI)-induced pitting damage in the rear wall of a typical Whipple shield (showing craters and cracks).

In lieu of traditional ultrasonic techniques, the nonlinear ultrasonic waves (NUWs)-based inspection, emerged in recent year, has proven to be able to detect and characterize the microstructural defects in their embryotic stage, in accordance with the fact that the damage introduces some degree of nonlinearity to the GUWs, which could be more sensitive than linear features to micro-scale damage[4-6]. Methods in this category are represented by those using the first-, second-, or sub-harmonics, mixed frequency responses, or shift in resonance frequency[7,8]. Most of these approaches address an abnormal intensification in material nonlinearity due to the enhancement of material plasticity, along with emergence of damage-induced contact acoustic nonlinearity (CAN)[9,10]. In general, the more severe the pitting damage is, the more significant the intensification in material nonlinearity and the more micro-cracks there will be.

Even though, it is challenging that some difficulties are confronted in the selection of the probing GUW mode and frequency because of the dispersive and multi-mode nature of GUWs in plate-like structures. Strict criteria have to be satisfied for the existence of NUWs to guarantee the accumulation of second-harmonic modes, including internal resonance condition, *i.e.*, phase-velocity matching, as well as non-zero power flux from fundamental modes to the secondary modes[11,12]. In addition, a third condition was given by Jacobs[13,14], which was referred to as group velocity matching, requiring equal group velocities of the fundamental and the secondary modes. However, there is still a dispute about the necessary of group-velocity matching. Generally, the dispersion curves of GUWs are an essential guide for the selection of optimal mode and frequency[15], and the NUWs exist only in particular frequencies, appearing in mode pairs. Theoretically there are an infinite number of mode pairs that satisfy the above two conditions, among which the mode pair (S1-s2) is most widely used. In practice, due to the deviation in the experimental equipment and device, as well as the operation during the detection process, the condition of exact phase velocity matching between the fundamental and the secondary modes is hardly to be satisfied. In addition, it may be difficult to generate the high frequency S1 mode by the lead zirconate titanate (PZT) wafers, which are used in the *in-situ* SHM system. Therefore, the low frequency mode pair (S0-s0) with approximate phase-velocity matching are mostly used for the evaluation of fatigue, thermal and creep damages.

To select a suitable mode pair, Jacobs[16], Lissenden[17] and Xiang[18] et al. compared the efficiency of GUW mode pairs that could generate the cumulative second-harmonic wave, which can be referred as excitation efficiency. The excitation efficiency is proposed as the basis of mode selection in the ultrasonic detection using NUWs. To improve the sensitivity and to enhance the reliability of the NUW-based pitting damage characterization, numerical models are developed for the analysis of the cumulative effect of second harmonics, including nonlinear SAFE approach to select the mode pairs and frequencies, and finite element (FE) models to simulate the accumulation of second harmonics. On this basis, an efficient mode pair and frequency is selected and practically applied to characterize the HVI-induced pitting damage in the rear wall of Whipple shields.

Downloaded From: https://www.spiedigitallibrary.org/conference-proceedings-of-spie on 07 Jul 2020
Terms of Use: https://www.spiedigitallibrary.org/terms-of-use

2. ANALYTICAL PRINCIPLE FOR MODE SELECTION

To better understand the generation and accumulation of high-order harmonics, and use them for evaluation of pitting damage, a dedicated modeling approach is developed. Consider an isotropic, homogeneous solid medium which is in its intact state, the nonlinearities in a propagating GUW originate from two major sources (during analytical derivation): the intrinsic material nonlinearity and the geometric (or convective) nonlinearity[10]; when the medium contains inherent imperfections (*e.g.*, lattice abnormality, precipitates and vacancies) or material lesion (*e.g.*, crack), additional nonlinearity will be embodied in the GUW. The intrinsic material nonlinearity refers to the intrinsic nonlinear elasticity of lattices, while the geometric nonlinearity is owing to the mathematic relation between the Eulerian coordinates and Lagrangian (material) coordinates. In the model, the nonlinearity is depicted using a three-dimensional (3-D) stress-strain relation with a second order approximation[6,12], as

$$\sigma_{ij} = (C_{ijkl} + 1/2\, M_{ijklmn}\varepsilon_{mn})\varepsilon_{kl}\,, \tag{1}$$

where $C_{ijkl} = \lambda\delta_{ij}\delta_{kl} + 2\mu I_{ijkl}$. σ_{ij} denotes the stress tensor, ε_{mn} and ε_{kl} the strain tensors, and C_{ijkl} the second-order elastic (SOE) tensor defined with Lamé parameter λ and μ. M_{ijklmn} is a tensor simultaneously accounting for the above two types of nonlinearities via

$$M_{ijklmn} = C_{ijklmn} + C_{ijln}\delta_{km} + C_{jnkl}\delta_{im} + C_{jlmn}\delta_{ik}\,, \tag{2}$$

where

$$\begin{aligned} C_{ijklmn} = &\frac{1}{2}\mathcal{A}(\delta_{ik}I_{jlmn} + \delta_{il}I_{jkmn} + \delta_{jk}I_{ilmn} + \delta_{jl}I_{ikmn}) \\ &+ 2\mathcal{B}(\delta_{ij}I_{klmn} + \delta_{kl}I_{mnij} + \delta_{mn}I_{ijkl}) + 2\mathcal{C}\delta_{ij}\delta_{kl}\delta_{mn}. \end{aligned} \tag{3}$$

In the above, C_{ijklmn} is the third-order elastic (TOE) tensor describing material nonlinearity, which is directly related to three TOE constants (*i.e.*, $\mathcal{A}$, $\mathcal{B}$ and $\mathcal{C}$). The last three terms of Equation (2) together address geometric nonlinearity. δ_{ik} and such in similar forms are the Kronecker deltas. I_{jlmn} and such in similar forms are the fourth-order identity tensors.

Based on the second order perturbation approximation, without considering the attenuation and dispersion, the second-harmonic field $u^{2\omega}(y,z)$ of GUWs can be expressed as[11],

$$u^{(2\omega)}(y,z) = \frac{1}{2}\sum_{m}^{\infty} A_m u_m^{2\omega}(y,z)e^{-i2\omega t} + c.c., \tag{4}$$

where $u^{2\omega}(y,z)$ is the field function and corresponding expansion coefficient of the mth second-harmonics. *c.c.* represents the complex conjugates. y and z denote the direction, as shown in the Figure 3. ω signifies the angular frequency of the probing GUWs excited at fundamental frequency. The amplitude of the second harmonic A_m is to quantify the contribution of the mth mode in the mode expansion, and it is given by[11],

$$A_m(z) = \bar{A}_m(z)\,\mathrm{e}^{i(2\kappa z)} - \bar{A}_m(0)\,\mathrm{e}^{i\kappa_n^* z}, \tag{5}$$

where κ_n^* is the complex conjugate of the wave number of the nth mode at 2ω. $\bar{A}_m$ can be expressed as,

$$\bar{A}_m(z) = \begin{cases} \dfrac{i(f_n^{vol} + f_n^{surf})}{4P_{mn}(\kappa_n^* - 2\kappa)}, & \text{if } \kappa_n^* \neq 2\kappa \text{(asymchronism)}, \\ \dfrac{(f_n^{vol} + f_n^{surf})}{4P_{mn}}z, & \text{if } \kappa_n^* = 2\kappa \text{(synchronism)}. \end{cases} \tag{6}$$

Downloaded From: https://www.spiedigitallibrary.org/conference-proceedings-of-spie on 07 Jul 2020
Terms of Use: https://www.spiedigitallibrary.org/terms-of-use

In the above, κ signifies the wave number of fundamental mode. P_{mn} is the complex power flux in direction $\boldsymbol{n_z}$ of the mth propagating mode in the expansion of the secondary solution. f_n^{vol} and f_n^{surf} denote driving force (*i.e.*, power flux) for the second harmonic waves generated through the volume and through the surface, respectively, due to the fundamental waves. Thus, a *nonlinear index NI* is defined to calibrate the nonlinearity in the medium, as,

$$NI = \frac{A_m^{2\omega}}{(A_m^{\omega})^2}. \tag{7}$$

where A_m^{ω} and $A_m^{2\omega}$ are the magnitudes of mth fundamental and second harmonic modes, respectively.

Assuming the probing GUW is transmitted at location $z = 0$, the amplitude of mth second harmonics can be expressed as,

$$A_m(z) = \frac{f_n^{vol}(z) + f_n^{surf}(z)}{4P_{mn}} \cdot \frac{c_p^{\omega} c_p^{2\omega}}{\omega(c_p^{2\omega} - c_p^{\omega})} \cdot \sin\left(\frac{\omega(c_p^{2\omega} - c_p^{\omega})}{c_p^{\omega} c_p^{2\omega}} \cdot z\right) \tag{8}$$

where c_p^{ω} and $c_p^{2\omega}$ denote the phase velocities of fundamental and second harmonic modes, respectively.

In the case of $\kappa_n^* = 2\kappa$, which denotes the phase-velocity matching ($c_p^{\omega} = c_p^{2\omega}$) between the fundamental and the second harmonic modes (as shown in Figure 2), if the power flux from fundamental modes to second harmonic modes is not zero ($f_n^{vol} + f_n^{surf} \neq 0$), $A_m(z)$ increases linearly along the propagation distance z. This is known as the "internal resonance (linear growth of second harmonics)", which requires two conditions: (1) phase-velocity matching ($c_p^{\omega} = c_p^{2\omega}$); (2) non-zero power transfer from the fundamental to the secondary wave fields ($f_n^{vol} + f_n^{surf} \neq 0$). For the mode pair with phase-velocity mismatching ($c_p^{\omega} \neq c_p^{2\omega}$) and non-zero energy flux ($f_n^{vol} + f_n^{surf} \neq 0$), as displayed in Figure 2, $A_m(z)$ remains bounded and oscillates with a spatial periodicity, often called the dispersion length z_n, which can expressed as,

$$z_n = \frac{2\pi}{|\kappa_n - 2\kappa|} = \frac{\pi}{2\omega} \frac{c_p^{\omega} c_p^{2\omega}}{\left|c_p^{2\omega} - c_p^{\omega}\right|}, \tag{9}$$

It can be found that z_n depends on the angular frequency and the phase velocities of the fundamental and second harmonic waves. When the quasi phase-velocity matching condition is satisfied, the propagation distance, within which the amplitude of the second harmonic mode grows cumulatively, may be large enough for material damage evaluation in practical applications.

As analyzed in the author's previous work[6,10,19], on top of a large quantity of macro-scale craters and cracks, diverse microstructural changes, for instance micro-voids, micro-cracks, recrystallized fine grains and dislocations, co-exist. These recrystallized fine grains, dislocation substructures and shock hardening jointly lead to an increase in material plasticity and hence intensification in material nonlinearity. In general, such intensification in material nonlinearity incurred by the pitting damage imposes remarkable influence on probing wave propagation more than the intrinsic material nonlinearity does. In the analytical model, the localized intensification in the material nonlinearity in the pitted region is depicted using the increasing in the three TOE constants (*i.e.*, $\alpha\mathcal{A}$, $\alpha\mathcal{B}$ and αC, α is the scale factor). According to the normal analysis[11], the increasing TOE constants contribute to the increase of the power fluxes f_n^{vol} and f_n^{surf}, resulting in the growth of the amplitude of the second harmonics $A_m(z)$, as illustrated in Equation (8).

Downloaded From: https://www.spiedigitallibrary.org/conference-proceedings-of-spie on 07 Jul 2020
Terms of Use: https://www.spiedigitallibrary.org/terms-of-use

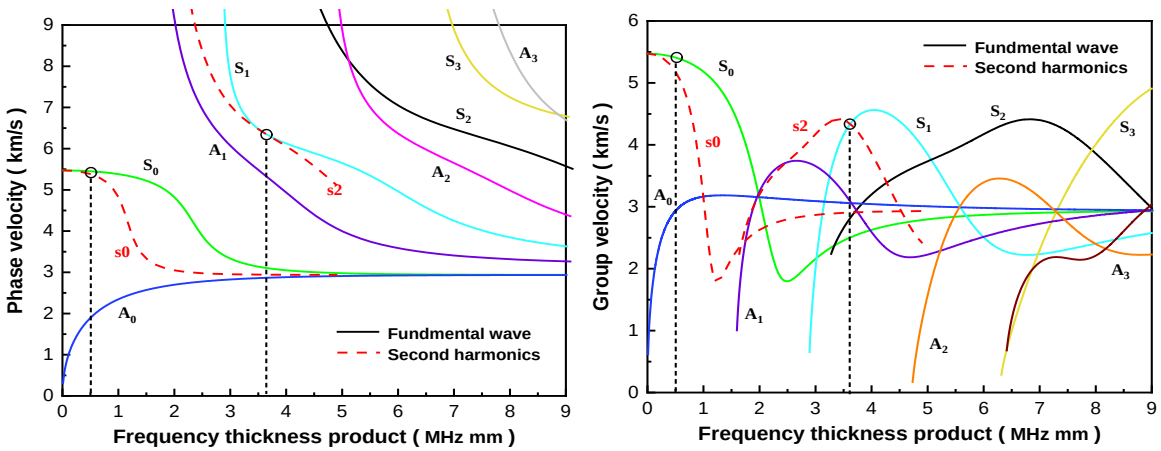

(a) (b)

Figure 2. Dispersion curves of 7075 aluminum plate (a) phase velocity; (b) group velocity.

In addition, numerous micro-voids expand to form micro-cracks and then macroscopic cracks, leading to the weakening of elastic constants. Simultaneously, interaction of a probing GUW with these cracks gives rise to the generation of CAN. The "breathing" behavior of micro-cracks introduce nonlinearities to scattered waves, serving as a secondary wave source located at the micro-crack – called "*crack-induced secondary source*" (*CISS* hereinafter) in the model, as detailed in the authors' earlier works[9,10]. *CISS* features time-dependent traits and initiate high-order harmonics. The in-plane displacement ($u_m^{S-2\omega}$) of *CISS*-induced m^{th}-order symmetric modes at the double excitation frequency (2ω) can be ascertained as[9,10]

$$u_m^{S-2\omega} = A_m^S u_m^S(y)\left[H_0^2(k_m r) - \frac{1}{k_m r} H_1^2(k_m r)\right], \tag{10}$$

where

$$A_m^S = \frac{k_m}{4i}\frac{2CISS_{in}^{bre-2\omega}\cdot u_m^S(0)}{I_{mm}^S}.$$

In the above, $u_m^{S-2\omega}$ signifies the *CISS*-induced in-plane displacement at 2ω (superscript S denoting the symmetric mode, and subscript n representing the mth order), $u_m^S(y)$ the in-plane displacement of wave mode as a function of y (see Figure 3), k_m the wave number of the propagating wave mode at 2ω, $H^2(\bullet)$ the Hankel function of the second kind, and r the distance from the crack to the sensor at which GUW is captured. A_m^S is the crack-induced wave fields at 2ω, i the imaginary unit, I_{mm}^S the energy carried by the GUW mode, and $u_m^S(0)$ the in-plane displacement of wave mode at the middle of the plate. $CISS_{in}^{bre-2\omega}$ is the in-plane component of $\overrightarrow{CISS}^{bre-2\omega}$ (the modulated *CISS* attributed to the "breathing" behavior at 2ω). The generation of the second harmonic of the probing GUW can be attributed to $\overrightarrow{CISS}^{bre-2\omega}$. With the CAN induced by the "breathing" behavior of micro-cracks in the pitted region, the second harmonic in GUW signals will be intensified, leading to a higher *NI*, as illustrated in Equation (7).

Downloaded From: https://www.spiedigitallibrary.org/conference-proceedings-of-spie on 07 Jul 2020
Terms of Use: https://www.spiedigitallibrary.org/terms-of-use

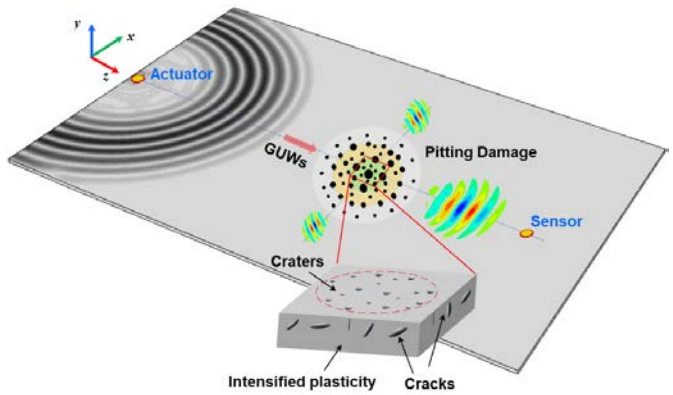

Figure 3. Illustration of NUW-based pitting damage detection (showing intensified plasticity, craters and cracks).

In the above analysis, the selection of optimal NUW modes for SHM is generally based on the known material properties and dispersion curves. However, the HVI induced-pitting damage will cause variations in the elastic constants of materials, such as the mass density and the elastic modulus, leading to the dispersion curves remain unclear. The effective Young's modulus $\overline{E}_p$ and Poisson's ratio $\overline{\mu}_p$ of the plate-like waveguide undergo pitting damage can be defined as[20],

$$\overline{E}_p = \frac{E(1-f_p)^2}{1+2\mu f_p} \tag{11}$$

$$\overline{\mu}_p = \frac{(1/4)(4\mu+3f_p-7\mu f_p)}{1+2f_p-3\mu f_p} \tag{12}$$

where f_p denotes the total micro-voids/cracks volume fraction in the microstructure of pitted region. Regarding to the plate-like structures, the dispersion equation can be expressed as,

$$\frac{\tanh(qh)}{\tanh(ph)} = -\left[\frac{4k^2pq}{(q^2-k^2)^2}\right]^{\pm 1}, \tag{13}$$

where the +1 is for the symmetric modes, while -1 is for the antisymmetric modes. h denotes half-thickness of the plate. In the dispersion Equation (13), $p=\sqrt{(\omega/c_L)^2-k^2}$ and $q=\sqrt{(\omega/c_T)^2-k^2}$, which is related to the bulk transverse velocity c_T and the bulk longitudinal velocity c_L, defined as follows,

$$c_T = \sqrt{\frac{\overline{E}_p}{2\rho(1+\overline{\mu}_p)}}, \tag{14}$$

$$c_L = \sqrt{\frac{\overline{E}_p(1-\overline{\mu}_p)}{\rho(1+\overline{\mu}_p)(1-2\overline{\mu}_p)}}, \tag{15}$$

Based on the Equations (11)-(15), it is noteworthy that the dispersion curves dependent on the Young's modulus and Poisson's ratio, which will be changed under variation of damage volume fraction. Accordingly, pitting damage leads to the deviation of dispersion curves, and thus the changing of phase-velocity matching condition. This phenomenon can be used as an indicator for selection of preferred mode pair to evaluate pitting damage.

Downloaded From: https://www.spiedigitallibrary.org/conference-proceedings-of-spie on 07 Jul 2020
Terms of Use: https://www.spiedigitallibrary.org/terms-of-use

In this Section, analytical model is developed to explore the modal properties and internal resonant conditions of NUWs in plate-like waveguides, which provides the theoretical basis for the investigation of mode sensitivity and analysis of interaction between incident GUWs and pitting damage.

3. PROOF-OF-CONCEPT USING A SAFE APPROACH

3.1 The accumulation effect of second harmonics

To validate the principle of proposed approach, finite element (FE) simulation is performed to explore the mode sensitivity and interaction between the probing GUW and pitting damage using ABAQUS®/EXPLICIT, in which the analytical solutions obtained in preceding section are recalled in a user-defined subroutine (VUMAT) – a SAFE approach. For convenience of following analysis, the dispersion curves of fundamental modes (S0, S1) and secondary modes (s0, s2) for the intact and damaged plate are calculated by SAFE using the material parameters are listed in Table 1 and separated from the other curves, as shown in Figure 4. The dispersion curves of the secondary modes (red and blue lines) are plotted overlapping with that of the fundamental modes, and point P is the equal point of phase velocities between the fundamental and the secondary modes. The dashed line and straight line represent the mode pairs for the damaged and intact plates, respectively. The crack density V_{crack} is defined as 0.01 in the theoretical model, which is corresponding to that observed in SEM[19]. A clear deviation of the dispersion curves with a change in damage volume fraction can be observed, indicating that some specific GUW modes, *i.e.*, the proper GUW modes and frequencies, are sensitive to pitting damage. It's noteworthy that the degree of phase-velocity mismatching increases in the damaged plate, which provides a basis for the selection of interested mode pair and frequency to evaluate pitting damage. The points (marked by solid circle) with different degrees of phase-velocity mismatching are selected for the subsequent analysis.

Table 1. Material parameter of Al7075 aluminum alloy.

Three TOE constants			Elastic modulus (GPa)	Poisson's ratio	Density (kg/m^3)	c_L (m/s)	c_T (m/s)
αA (GPa)	αB (GPa)	αC (GPa)					
-351.2	-149.4	-102.8	73.1	0.34	2757.82	6372.70	3146.18

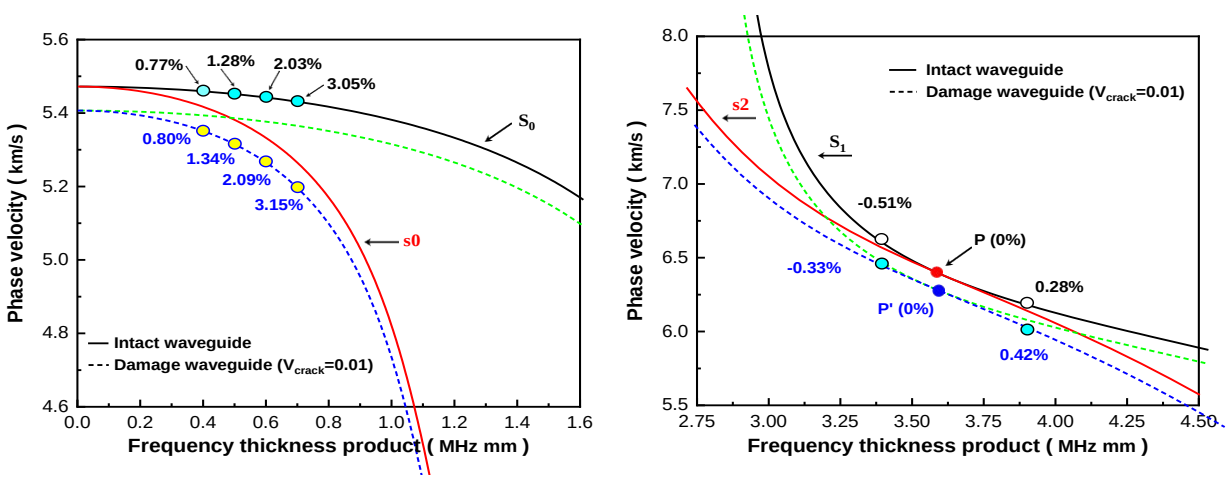

(a) (b)

Figure 4. The phase velocity dispersion curves of intact structure and damaged structure: (a) S0-s0 mode pair; (b) S1-s2 mode pair.

Downloaded From: https://www.spiedigitallibrary.org/conference-proceedings-of-spie on 07 Jul 2020
Terms of Use: https://www.spiedigitallibrary.org/terms-of-use

In the simulation, two-dimensional (2-D) FE models for both the intact and damaged aluminum plates (2 mm in thickness, 1000 mm long) are developed, as displayed in Figure 5, and the models are discretized with the four-node plane strain (CPE4R) elements. A ten-cycle Hanning-windowed sinusoidal tone-burst at different excitation frequencies are applied to generate the two selected mode pairs, viz., S0-s0 at a lower frequency range and S1-s2 at a higher frequency range. To excite an appropriate probing GUWs, the in-plane displacement of the same amplitude (1×10^{-4} mm) in parallel with the waveguide surface is applied to the left edge of the plate, and under this condition only the symmetric wave modes are generated. To warrant simulation accuracy, a fine mesh with an element size of 0.1 mm and 0.05 mm is applied in the model for the mode pairs S0-s0 and S1-s2, respectively. GUW propagation in the waveguide is continuously monitored by measuring the in-plane displacements of the plate surface every 10 mm. The in-plane displacements of both the 0° phase and 180° out-of-phase inverted GUWs are extracted at the measurement points and processed with an pulse-inversion approach, with which the weak nonlinearity (*i.e.*, $A_m^{2\omega}$ in Equation (7)) stands out in the superimposed signals and in spectra (obtained via the short-time Fourier Transform (STFT)).

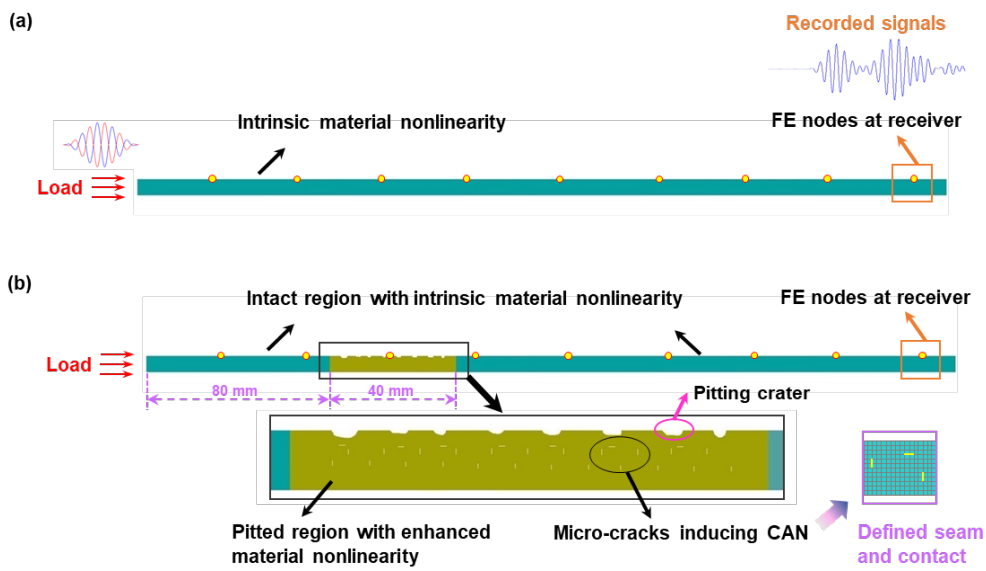

Figure 5. 2-D FE model of the plate-like waveguide: (a) intact plate; (b) damaged plate.

For the intact plate, combining the use of SAFE approach and FE simulations, the accumulation effect of interested second harmonics is demonstrated in Figure 6. Regardless of the excitation frequency, the *NI* oscillates along the propagation distance in a sinusoidal behavior for the mode pair S0-s0 – a phenomenon that can be attributed to the inaccurate matching in the respective phase and group velocities of two modes (as seen in Figures 2 and 4). With the increasing of excitation frequency, the degree of phase-velocity is intensified, leading to the decreasing of the oscillation spatial period, as shown in Figure 6(a). Considering the S1-s2 mode pair satisfied the phase-velocity matching condition, *NI* shows a monotonic and linear increase over the propagation distance, as displayed in Figure 6(b). While *NI* also oscillates along the propagation distance in a sinusoidal behavior when the phase-velocity is not matched. The oscillation amplitude and spatial period are consistent between the simulation results and the SAFE analysis, which is theoretically acquired by Equations (4) and (8), as shown in Table 2. The *NI* grows cumulatively with the propagation distance within half the oscillation spatial period z_n. Note that z_n can be calculated using Equation (9), which is inversely proportional to the deviation of the phase velocities between the fundamental and second harmonic modes. It's noteworthy that in the intact plate, the second harmonics are generated and accumulated owning to the intrinsic material nonlinearity (represented by the TOE constants).

Downloaded From: https://www.spiedigitallibrary.org/conference-proceedings-of-spie on 07 Jul 2020
Terms of Use: https://www.spiedigitallibrary.org/terms-of-use

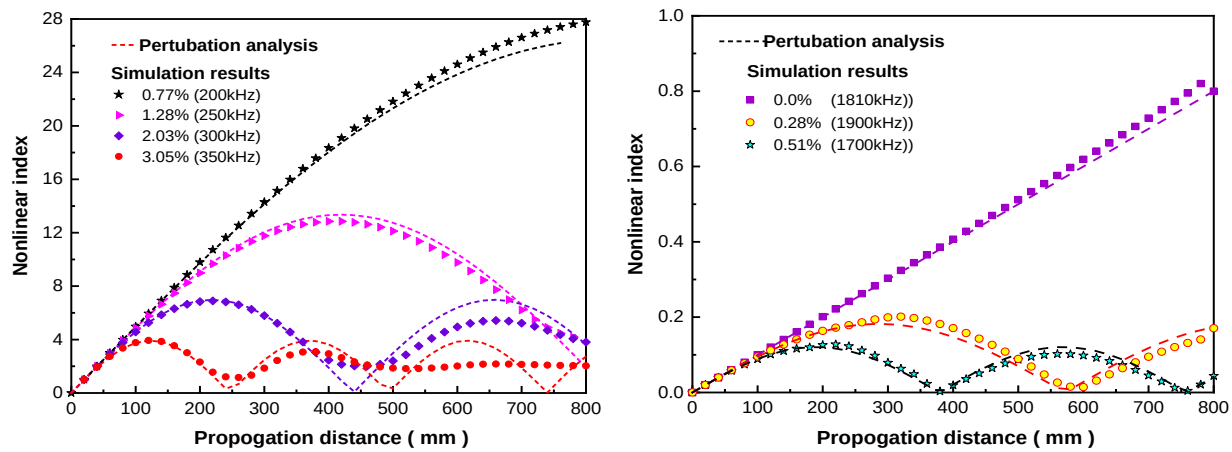

(a) (b)

Figure 6. Comparison of *NI* obtained by SAFE analysis and simulations for the intact plate: (a) S1-s0 mode pair; (b) S1-s2 mode pair.

3.2 Mode sensitivity of characterizing pitting damage

Regarding the damaged plate, the SAFE analysis is firstly conducted, considering the crack-induced deterioration of elastic constants of material and intensification of material plasticity, respectively. It's noteworthy that accumulation effect of second harmonics in the damaged plate is similar to that of the intact plate, as demonstrated in Figure 7 and Table 2. The dispersion distance z_n decreases in the damaged plate with cracks, due to the intensification of phase-velocity mismatching, which is caused by the weakened elastic constants of material. In addition, with the CAN induced by the "breathing" behavior of micro-cracks, the second harmonic in GUWs is intensified, leading to a higher *NI*, as illustrated in Equations (7) and (10). While the z_n obtained in the damaged plate with enhanced material plasticity is consistent with that of the intact plate, because the second-order elastic constants of this plate are assumed to remain unchanged in the SAFE method. The increasing TOE constants ($\alpha\mathcal{A}$, $\alpha\mathcal{B}$ and αC) contribute to the increase of the power fluxes f_n^{vol} and f_n^{surf}, resulting in a slight growth of the *NI*, as illustrated in Equations (7) and (8). To weaken the accumulation effect of material nonlinearity, and stand out the crack-induced CAN, the low frequency mode pair S0-s0 are more suitable for the pitting damage evaluation.

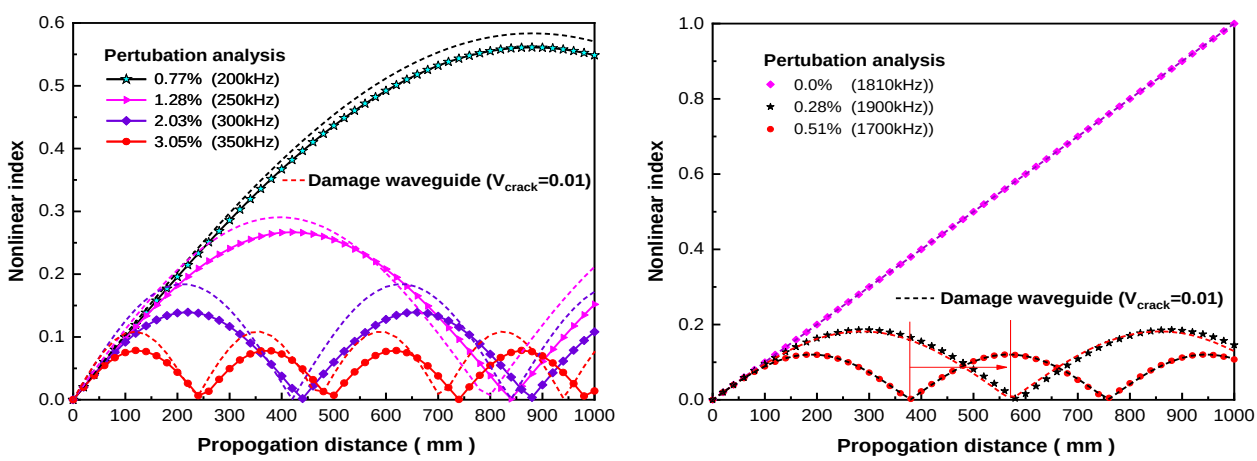

(a) (b)

Downloaded From: https://www.spiedigitallibrary.org/conference-proceedings-of-spie on 07 Jul 2020
Terms of Use: https://www.spiedigitallibrary.org/terms-of-use

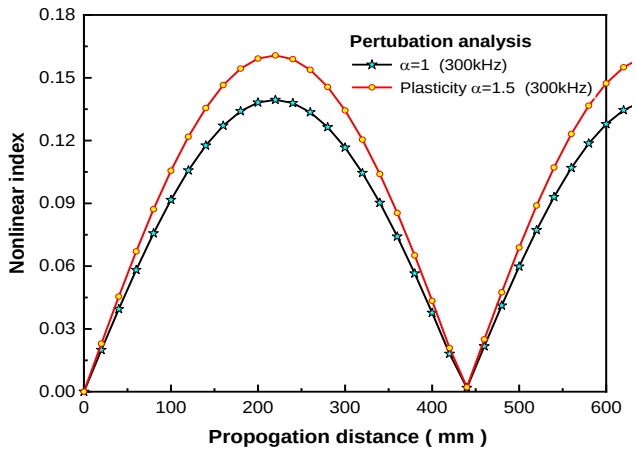

(c)

Figure 7. Comparison of *NI* obtained in the intact and damaged plate by SAFE analysis: (a) damaged plate with cracks using the S1-s0 mode pair; (b) damaged plate with cracks using the S1-s2 mode pair; (c) damaged plate with enhanced material plasticity using the S1-s0 mode pair.

Table 2. Results obtained by SAFE approach for the intact and damaged plates.

Mode pair	Excitation frequency (kHz)	Plate	Phase velocity (m/s)	Mismatch degree (%)	Dispersive distance
S0-s0	200	Intact	5459-5417	0.70	1.76
		Damaged	5394-5351	0.80	1.76
	250	Intact	5452-5382	1.28	0.84
		Damaged	5387-5315	1.34	0.80
	300	Intact	5443-5333	2.03	0.44
		Damaged	5377-5264	2.09	0.42
	350	Intact	5431-5265	3.05	0.25
		Damaged	5365-5196	3.15	0.24
S1-s2	1810	Intact	6374-6258	0	--
		Damaged	6258-6258	0	--
	1700	Intact	6597-6564	0.51	0.38
		Damaged	6463-6442	0.33	0.57
	1900	Intact	6242-6224	0.28	0.58
		Damaged	6136-6110	0.42	0.38

Downloaded From: https://www.spiedigitallibrary.org/conference-proceedings-of-spie on 07 Jul 2020
Terms of Use: https://www.spiedigitallibrary.org/terms-of-use

To validate the predictions from the nonlinear SAFE method, FE simulations for the plate with pitting damage are also carried out in a similar way with that of the intact plate. In the simulations, a pitted region of a diameter of 40 mm is 80 mm to the left boundary of the plate, containing three types of nonlinear sources, *i.e.*, the intrinsic and plasticity-induced material nonlinearity, and CAN, as shown in Figure 5(b). Ten craters with a diameter of 0.6 mm for each are uniformly distributed at the surface of the pitted region at an interval of 4 mm. To model the intensified material nonlinearity in the pitted region, the TOE constants increase equally up to $\alpha\mathcal{A}$, $\alpha\mathcal{B}$ and αC for this region, where the scale factor α is assumed to be 1.5 (compared with 1.0 for an intact waveguide) according to large volume compression of the material (35~50%) that is caused by debris cloud impact[19]. Modeling of intrinsic and intensified material nonlinearities is implemented in VUMAT using the nonlinear stress-strain relation. To model the micro-cracks beneath the craters in the pitted region, N ($N = 20$) seam cracks with a length of a ($a = 0.2\,\text{mm}$) for each are defined and distributed uniformly with an area S, as seen in Figure 5(b). To be consistent with experimental configuration in the following, ten seam cracks in parallel with the waveguide surface are defined beneath the ten craters, along with other cracks along the thickness direction. A contact-pair interaction definition, which prohibits the penetration of nodes into opposite surface is imposed on the two contacting interfaces for each micro-crack for describing the "breathing" behavior when probing GUWs traverse. The crack density V_{crack} is calculated to be 0.01 using a dimensionless parameter $V_{crack} = Na^2 / S$.

The simulation results are analyzed and discussed in a similar way with that of the intact plate, as displayed in Figure 8. The *NI* is normalized by the peak value of the intact plate, marked by the dash line. Compared with the results from the intact plate, the *NI* obtained in the plate with pitting damage is increased phenomenally. It is noteworthy that among various sources of nonlinearity, the intensification of material nonlinearity due to plasticity-driven damage is stronger than that of the intrinsic material nonlinearity, while it is much weaker than that arising from "breathing" cracks-induced CAN. Together, both of the intrinsic and intensified material plasticity, and "breathing" cracks jointly give rise to the accumulation of second harmonics in the waveguide bearing pitting damage. The accumulation effect of second harmonics against the propagation distance in simulations for the intact and damaged plate are similar to that of the SAFE analysis. To further analyze the sensitivity of mode pairs at different excitation frequencies, the normalized *NIs* of mode pairs obtained at the excitation frequencies of 200 kHz, 250 kHz, 300 kHz and 350 kHz are compared. Regardless of the selected mode pairs, the *NI* obtained in the pitted plate (with intensified material plasticity, and "breathing" cracks-induced CAN) is observed to increase significantly after the probing GUWs traverse the pitted region. This phenomenon is remarkable particularly when the degree of phase-velocity mismatching is intensified. It is noteworthy that with the increasing degree of phase-velocity mismatching, the accumulation effect of material nonlinearity is weakened. While the the pitting damage-induced nonlinearity stands out with comparable effectiveness, in particular the crack-induced CAN. Thus, the mode pair S0-s0 at a relatively higher degree of phase-velocity mismatching is more sensitive to characterize the pitting damage.

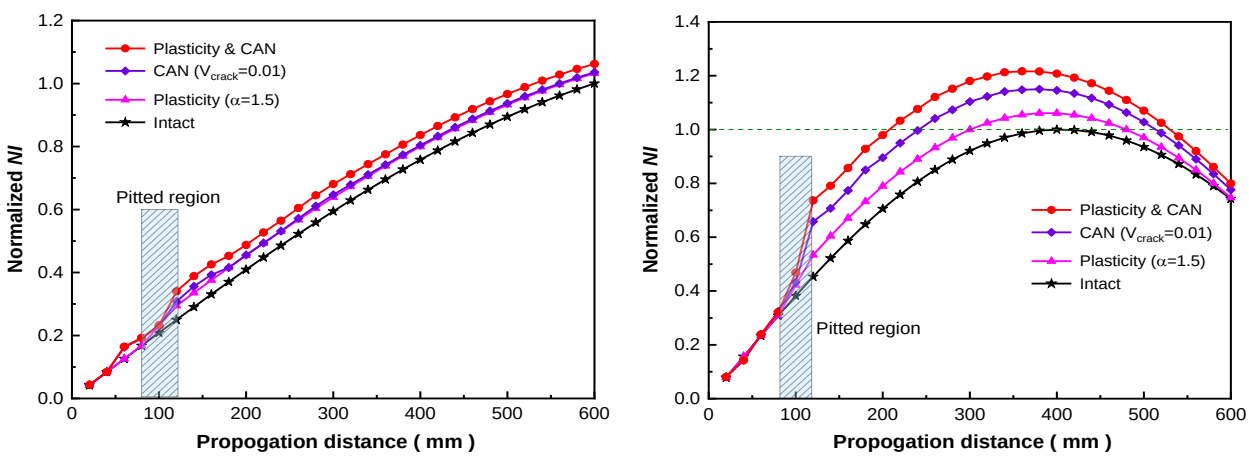

(a) (b)

Downloaded From: https://www.spiedigitallibrary.org/conference-proceedings-of-spie on 07 Jul 2020
Terms of Use: https://www.spiedigitallibrary.org/terms-of-use

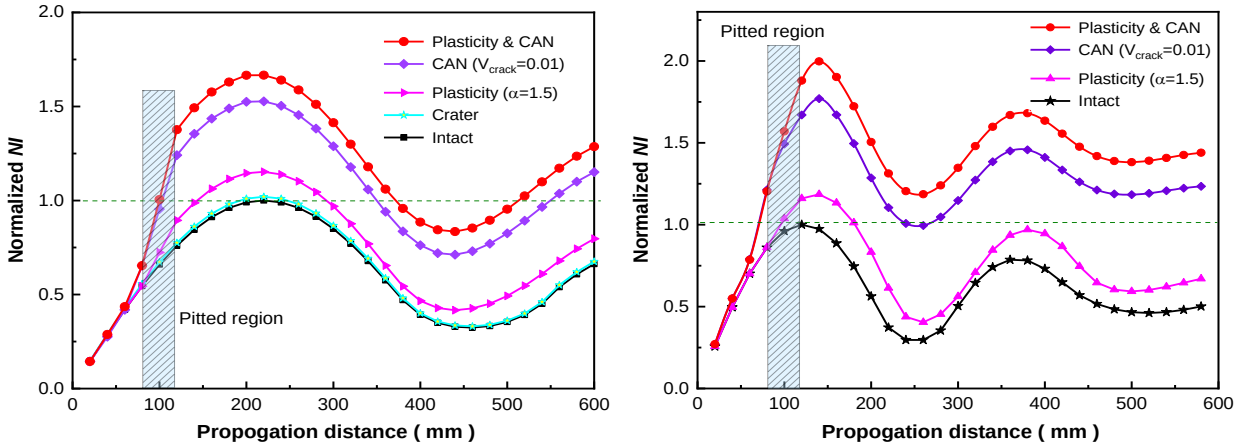

(c) (d)

Figure 8. Comparison of normalized *NI* obtained using the mode pair S0-s0 with different excitation frequencies: (a) 200 kHz; (b) 250 kHz; (c) 300 kHz; (d) 350 kHz.

4. EXPERIMENTAL VALIDATION

To validate the feasibility of selected mode pair, S0-s0 mode pair with different degree of phase-velocity mismatching is applied to characterize the HVI-induced pitting damage in the rear wall of Whipple shields.

4.1 Experimental set-up

To create the pitting damage in the rear wall of Whipple shields, HVI tests are conducted using a two-stage light gas gun. In the test, a spherical projectile (AL-2017, Ø 3.2 mm) is accelerated to 4.13 km/s to impact the typical dual-layered Whipple shield, which consists of a bumper layer (2024-T4, 1 mm in the thickness) and a rear wall layer (5A06, 3 mm in the thickness, 500 mm × 500 mm in the in-plane dimension) with a shield spacing of 100 mm, as seen in Figure 9(a). The bumper layer is penetrated by the projectile due to the vast kinetic energy, and some portions of the bumper layer are jetted, forming a debris cloud with shattered projectile, which further impacts the rear wall layer. Consequently, pitting damage, featuring multitudinous small-scale craters and cracks, are induced and disorderedly clustered over a large area.

After the HVI experiment, the pitting damage are characterized using nonlinear features of selected mode pair. In the tests, 22 miniaturized, lightweight piezoelectric wafers (PZT) wafers (PSN33, Φ5 mm, thickness: 0.48 mm) are mounted on surface of the rear wall layer to form eleven sensing paths covering the pitted region, as shown in Figure 9(b). The sensing path is 160 mm in length with an interval of 10 mm to each other. A computer controlled system (RITEC RAM-5000 SNAP) is used to generate a 10-cycle Hanning-windowed sinusoidal tone-burst signal, which is then input to the filter to filter out the undesired nonlinearities caused by the system before being fed to the PZT. The mode pair S0-s0 with various excitation frequencies as investigated in preceding SAFE-based analysis are generated via this system. The response voltage signals are acquired by an oscilloscope (Agilent DSO 9064A) and averaged 256 times to minimize measurement uncertainty. The procedure of signal processing remains the same with that of the FE simulation.

Downloaded From: https://www.spiedigitallibrary.org/conference-proceedings-of-spie on 07 Jul 2020
Terms of Use: https://www.spiedigitallibrary.org/terms-of-use

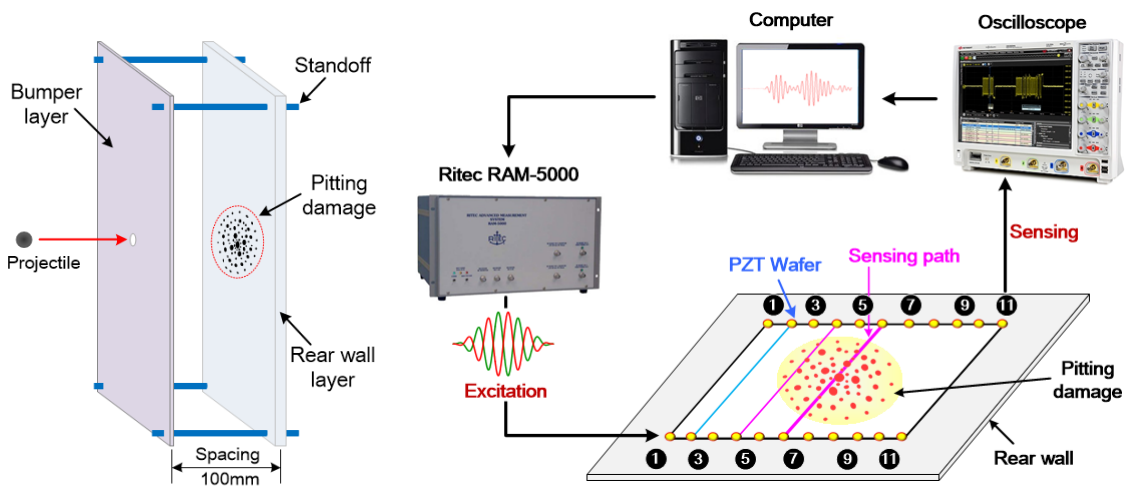

(a) (b)

Figure 9. (a) Schematic of a typical dual-layered Whipple shield; (b) schematic of nonlinear ultrasonic experiment.

4.2 Results and discussion

A representative wave signal captured via the sensing path six traversing the center of pitting damage region is displayed in Figure 10(a). After processing the obtained wave signal using STFT, the magnitudes of the fundamental and secondary modes can be ascertained, as shown in Figure 10(b), on which basis *NI* can be calculated according to Equation (7). The spectra of the extracted second harmonic signals obtained via two representative sensing paths (path one and path six), when the path is intact and contains pitting damage, respectively, are displayed in Figures 10(c) and (d), respectively. It can be observed that the incident energy of probing GUW shifts from the fundamental mode to the second harmonic mode significantly in the damaged path.

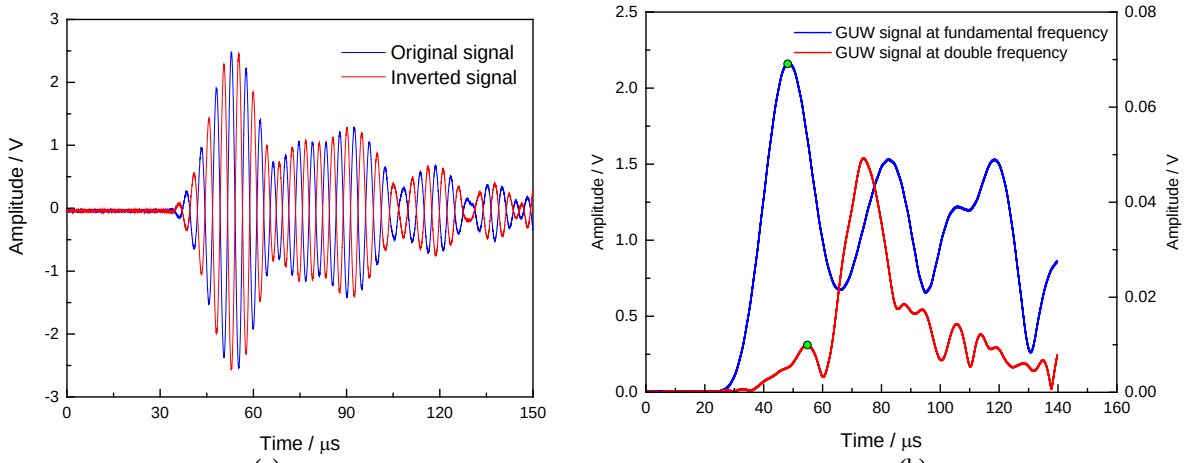

(a) (b)

Downloaded From: https://www.spiedigitallibrary.org/conference-proceedings-of-spie on 07 Jul 2020
Terms of Use: https://www.spiedigitallibrary.org/terms-of-use

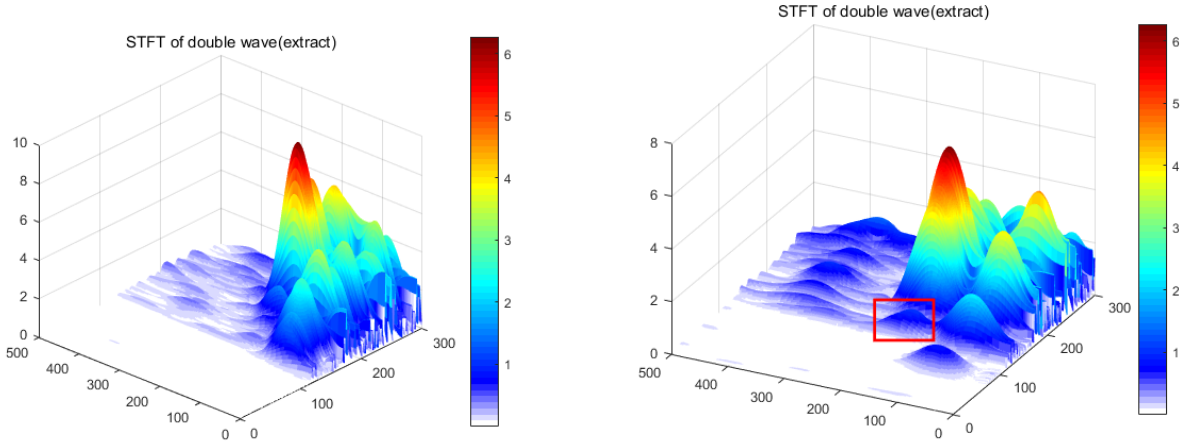

(c) (d)

Figure 10. (a) Representative wave signal obtained from the sensing path six; (b) magnitudes of the fundamental and secondary modes via the sensing path six, respectively; (c) and (d) spectrum at double excitation frequency of wave signal from the sensing paths one and six , respectively

To further analyze the sensitivity of mode pair S0-s0 for characterization of pitting damage, the *NIs* of mode pair S0-s0 with different excitation frequencies (*i.e.*, 200 kHz, 250 kHz, 300 kHz and 350 kHz) are normalized by the value of *NI* obtained in the intact path, and then compared, as presented in Figure 11(b). The *NI* increases with the intensification of pitting damage. In addition, with the increasing degree of phase-velocity mismatching (or excitation frequency), the *NI* gradually grows, which is consistent with the theoretical and SAFE analysis. Therefore, a higher excited frequency is preferred for mode pair S0-s0 to characterize the pitting damage.

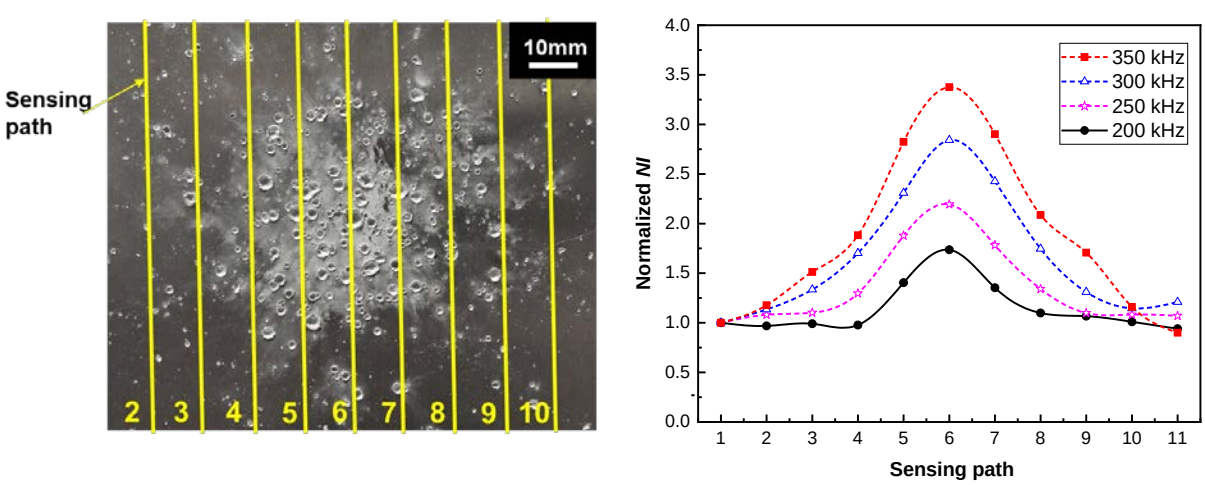

Figure 11.(a) Photography of the rear wall with pitting damage (showing the sensing path); (b) comparison of normalized *NI* obtained using mode pair S0-s0 with different excitation frequencies.

5. CONCLUSIONS

In this paper, numerical models are developed for the analysis of nonlinear guided waves in plate-like waveguides with pitting damage, including SAFE approach to identify internal resonant condition and select an efficient mode pair, and FE simulations to gain an insight into the generation of nonlinear features in GUWs at different excitation frequencies.

Downloaded From: https://www.spiedigitallibrary.org/conference-proceedings-of-spie on 07 Jul 2020
Terms of Use: https://www.spiedigitallibrary.org/terms-of-use

Regardless of the selection of mode pair (*i.e.*, S1-s2 and S0-s0), the amplitude of second harmonics obtained in the pitted plate (with intensified material plasticity, and micro-cracks-induced CAN) is observed to increase significantly after the probing GUWs traverse the pitted region, upon interacting with the pitting damage. This phenomenon is remarkable particularly when the probing GUW does not satisfy the requirement of internal resonance. The excited frequency selection is further analyzed in a certain frequency range to explore the mode sensitivity for characterizing the pitting damage, where the quasi phase-velocity matching condition is satisfied for mode pair S0-s0, and corroborated by experiment. Results show that the highly complex pitting damage in the Whipple shield of spacecraft, engendered by a hypervelocity debris cloud, can be effectively detected using the mode pair S0-s0, and a relatively higher excited frequency is preferred due to its higher degree of phase-velocity mismatching, leading to stand out of the pitting damage-induced CAN.

ACKNOWLEDGMENTS

This project was funded by the National Natural Science Foundation of China (Nos. 51875492, 51635008 and 11772113) and the Hong Kong Research Grants Council via General Research Fund (Nos. 15201416, 15212417 and 15204419).

REFERENCES

[1] Karl, T., "Space.com," 02 October 2013, https://www.space.com/23039-space-junk-explained-orbital-debris-infographic.html (19 March 2020).
[2] Christiansen, E. L., Hyde, J. L., Bernhard, R. P., "Space shuttle debris and meteoroid impacts," Adv Space Res 34(5), 1097-1103 (2004).
[3] Valluri, J.S., et al., "Creep damage characterization using non-linear ultrasonic techniques," Acta Mater 58(6),2079-90 (2010).
[4] Jhang, K. Y., "Nonlinear ultrasonic techniques for nondestructive assessment of micro damage in material: a review," Int J Precision Eng Manuf 10 (1),123-35 (2009).
[5] Liu, M., et al. "Characterizing Hypervelocity Impact (HVI)-induced pitting damage using active guided ultrasonic waves: from linear to nonlinear," Materials 10(5), 547 (2017)
[6] Cao, W., Zhou, P., Wang, K., et al., "Quantitative characterization of hypervelocity debris cloud-induced pitting damage in AL-Whipple shields using nonlinear ultrasonic waves," Proc. ISWHM, (2019).
[7] Wang, X., Wang, X., Hu, X., et al.," Damage assessment in structural steel subjected to tensile load using nonlinear and linear ultrasonic techniques," Appl Acoust, 144, 40-50 (2019).
[8] Dutta, D., Sohn, H., Harries, K. A., et al., "A nonlinear acoustic technique for crack detection in metallic structures," Struct Health Monit 8(3), 251-262 (2009).
[9] Wang, K., Liu, M., Su, Z., et al., "Analytical insight into "breathing" crack-induced acoustic nonlinearity with an application to quantitative evaluation of contact cracks," Ultrasonics, 88,157-167 (2018).
[10] Wang, K., Li, Y., Su, Z., et al., "Nonlinear aspects of "breathing" crack-disturbed plate waves: 3-D analytical modeling with experimental validation," Int J Mech Sci 159, 140-150 (2019).
[11] Deng, M., "Analysis of second-harmonic generation of Lamb modes using a modal analysis approach," Appl. Phys Lett 94(6), 4152 (2003).
[12] De Lima, W. J. N., Hamilton, M. F., "Finite-amplitude waves in isotropic elastic plates," J. Sound Vib 265(4), 819-839 (2003).
[13] Bermes, C., Kim, J. Y., Qu, J. M., Jacobs, L. J., "Experimental characterization of material nonlinearity using Lamb waves." Appl Phys Lett 90(2), 2067-2073 (2007).
[14] Müller, M.F., Kim, J.Y., Qu, J.M., Jacobs, L. J., "Characteristics of second harmonic generation of Lamb waves in nonlinear elastic plates," J Acoust Soc Am 127(4), 2141-52 (2010).
[15] Li, F., Sun, X., Qiu, J., et al., "Guided wave propagation in high-speed train axle and damage detection based on wave mode conversion," Struct Health Monit 22(9), 1133-1147 (2015).

Downloaded From: https://www.spiedigitallibrary.org/conference-proceedings-of-spie on 07 Jul 2020
Terms of Use: https://www.spiedigitallibrary.org/terms-of-use

[16] Matlack, K. H., Kim, J.Y., Jacobs, L. J., Qu, J. M., "Experimental characterization of efficient second harmonic generation of Lamb wave modes in a nonlinear elastic isotropic plate," J Appl Phys 109(1), 2141 (2011).
[17] Liu, Y., Chillara, V. K., Lissenden, C.J., "On selection of fundamental modes for generation of strong internally resonant second harmonics in plate," J Sound Vib 332(19), 4517-4528 (2013).
[18] Zhao, S., Deng, M., Xiang, Y., Xuan, F., "Excitation efficiency analysis and mode selection on second harmonic generation of ultrasonic Lamb waves," Acta Acustica 42(3), 290-296 (2017).
[19] Cao, W., Wang, Y., Zhou, P., et al., "Microstructural material characterization of hypervelocity-impact-induced Pitting Damage," Int J Mech Sci, 163, 105097 (2019).
[20] Cao, W., Pang, B., Su, Z., et al., "Modeling of ultrasonic nonlinearities for debris cloud-induced micro-voids characterization: theoretical analysis and numerical validation," Proc. SPAWDA, 1-5 (2019).

Downloaded From: https://www.spiedigitallibrary.org/conference-proceedings-of-spie on 07 Jul 2020
Terms of Use: https://www.spiedigitallibrary.org/terms-of-use